

Extended ductility due to kink band formation and growth under tensile loading in single crystals of Mg-Zn-Y alloy with 18R-LPSO structure

Takagi, Kosuke; Mayama, Tsuyoshi; Mine, Yoji; Chiu, Yu-Lung; Takashima, Kazuki

DOI:

[10.1016/j.jallcom.2019.07.344](https://doi.org/10.1016/j.jallcom.2019.07.344)

License:

Creative Commons: Attribution-NonCommercial-NoDerivs (CC BY-NC-ND)

Document Version

Peer reviewed version

Citation for published version (Harvard):

Takagi, K, Mayama, T, Mine, Y, Chiu, Y-L & Takashima, K 2019, 'Extended ductility due to kink band formation and growth under tensile loading in single crystals of Mg-Zn-Y alloy with 18R-LPSO structure', *Journal of Alloys and Compounds*, vol. 806, pp. 1384-1393. <https://doi.org/10.1016/j.jallcom.2019.07.344>

[Link to publication on Research at Birmingham portal](#)

Publisher Rights Statement:

Tagaki, K. et al, Extended ductility due to kink band formation and growth under tensile loading in single crystals of Mg-Zn-Y alloy with 18R-LPSO structure, *Journal of Alloys and Compounds*, vol. 806, pages 1384-1393, DOI: 10.1016/j.jallcom.2019.07.344

General rights

Unless a licence is specified above, all rights (including copyright and moral rights) in this document are retained by the authors and/or the copyright holders. The express permission of the copyright holder must be obtained for any use of this material other than for purposes permitted by law.

- Users may freely distribute the URL that is used to identify this publication.
- Users may download and/or print one copy of the publication from the University of Birmingham research portal for the purpose of private study or non-commercial research.
- User may use extracts from the document in line with the concept of 'fair dealing' under the Copyright, Designs and Patents Act 1988 (?)
- Users may not further distribute the material nor use it for the purposes of commercial gain.

Where a licence is displayed above, please note the terms and conditions of the licence govern your use of this document.

When citing, please reference the published version.

Take down policy

While the University of Birmingham exercises care and attention in making items available there are rare occasions when an item has been uploaded in error or has been deemed to be commercially or otherwise sensitive.

If you believe that this is the case for this document, please contact UBIRA@lists.bham.ac.uk providing details and we will remove access to the work immediately and investigate.

Extended ductility due to kink band formation and growth under tensile loading in single crystals of Mg-Zn-Y alloy with 18R-LPSO structure

Kosuke Takagi^a, Tsuyoshi Mayama^a, Yoji Mine^a, Yu Lung Chiu^b, Kazuki Takashima^a

^a *Department of Materials Science and Engineering, Kumamoto University, 2-39-1 Kurokami, Chuo-ku, Kumamoto 860-8555, Japan*

^b *School of Metallurgy and Materials, University of Birmingham, Edgbaston, Birmingham B15 2TT, United Kingdom*

Abstract:

The deformation behaviour of single crystals of an $\text{Mg}_{85}\text{Zn}_6\text{Y}_9$ alloy with an 18R-LPSO structure was experimentally and numerically investigated using a micro-tensile testing method and a crystal plasticity finite element method, respectively. The deformation microstructure was characterised using optical and electron microscopy. The experimental results indicated that kink band was formed in the specimens depending on the initial crystal orientation relative to the loading direction. The kink banding was accompanied with remarkable ductility of over 50% nominal strain. The deformation behaviour observed was successfully reproduced in a crystal plasticity finite element analysis. The numerical results indicated that the kink band was formed by the accumulation of basal slip, which was enhanced by the geometrical softening owing to the lattice rotation. The growth of a kink band, which was reasonably explained by the changes in Schmid factor for a basal slip system due to lattice rotation, suppressed the localised failure at low strain. This resulted in the observed extended ductility, even in the LPSO structure with strong plastic anisotropy.

Keywords: mechanical properties; anisotropy; intermetallics; metals and alloys; dislocations and disclinations; transmission electron microscopy, TEM

1. Introduction

Magnesium (Mg) alloys containing the secondary phase with a long-period stacking ordered (LPSO) structure (LPSO-type Mg alloys) have attracted considerable attention because of their high strength and reasonable ductility [1]. Figure 1 shows a

structural model of 18R-type LPSO phase in Mg-Zn-Y alloy, which has been previously proposed [2–4]. The LPSO structure has close-packed (0001) plane as same to an α -Mg with hexagonal closed-packed (HCP) structure. However, period of stacking sequence of (0001) planes along c -axis is increased up to 18-fold in 18R-type LPSO phase as compared to 2-fold in the α -Mg. The 18R structure has periodic chemical modulation of solute atoms, Zn and Y, which are distributed across the four close-packed layers. In addition, stacking faults are formed at every six HCP stacking layers, locating in the middle of Zn/Y enriched layers. Several studies [5, 6] have suggested the significant contribution of the LPSO phase to high strength in LPSO-type Mg alloys, which has led to academic interest in the LPSO structure. Extensive studies on the deformation behaviour of the LPSO structure have revealed the frequent formation of kink bands in plastically deformed alloys [7–18]. Recently, Hagihara et al. [19] quantitatively elucidated a close relationship between the high strength of the LPSO structure and kink band formation. Therefore, the introduction of a large amount of kink bands during the metal forming process can improve the mechanical properties of these alloys, which requires a detailed understanding of the underlying mechanism for kink band formation. To gain this understanding, numerical investigations of compressive kinking have been performed [20–23], which revealed the effects of the material properties, initial crystal orientation, and boundary conditions on kink band formation. However, kink band formations in an LPSO structure under loadings other than compression have not been examined thus far.

In addition to the Mg-based LPSO structure, kink bands are frequently observed in various solid materials [24–32]. For metallic materials, Orowan published a pioneering paper on kink band formation in a Cd crystal [24], where the possibility of kinking under both tension and compression in general crystalline materials was mentioned. Later, tensile kinking was experimentally observed in various materials including Zn [33, 34], Al [35], Cd [36], and Fe [37]. However, the detailed formation process and the effective parameters for tensile kinking were not investigated.

In recent studies, nanolamellar materials such as pearlitic steel [38] and Cu-Nb [39, 40] showed kink mode deformation when they were subjected to compressive loading in-lamellar-plane direction. Notably, Nizolek et al. [39] concluded that kink band formation enhances the deformability of nanocrystalline metals where dislocation motion is strongly confined. This insight suggests a possible relationship between kink

band formation and ductility, even in LPSO structures where the activity of non-basal dislocations is limited.

In this study, the deformation behaviour of single crystals of an $\text{Mg}_{85}\text{Zn}_6\text{Y}_9$ alloy with an 18R-LPSO structure was experimentally investigated using a micro-tensile testing method developed by Mine et al. [41–43]. The deformation microstructure was characterised using optical and electron microscopy, with a focus on the crystallographic orientation dependence of the deformation band formation. The underlying deformation mechanism relating to kink-mode deformation banding was numerically investigated via crystal plasticity finite element analysis. Finally, the relationship between the kink band formation and ductility in the LPSO structure was discussed according to the experimental and numerical results.

2. Experimental procedure

The material used in this study was a directionally solidified (DS) $\text{Mg}_{85}\text{Zn}_6\text{Y}_9$ (at.%) alloy produced via the Bridgeman method. Figure 2a shows a back scattered electron image of the microstructure of the DS $\text{Mg}_{85}\text{Zn}_6\text{Y}_9$ alloy observed in the transverse section with respect to the crystal growth direction. The microstructure of the alloy consisted of LPSO single-phase plates with an average thickness of $\sim 100\text{ }\mu\text{m}$. Micro-tensile specimens with gauge section dimensions of approximately $20 \times 20 \times 50\text{ }\mu\text{m}^3$ (Fig. 2b) were fabricated using a focused ion beam (FIB). Single-crystalline specimens with different crystal orientations relative to the loading direction (LD) were prepared, where the crystal orientation was measured using the electron backscatter diffraction (EBSD) technique. Details regarding the specimen preparation are described elsewhere [41]. For the prepared samples, the angles between the LD and the [0001] direction, which is denoted as ϕ in this study, were 14° , 30° , 45° , 60° , and 70° . Here, [0001] direction and an a -axis are laid on LD-TD plane, which leads to activation of single variant of basal slip system and the resultant in-plane plastic deformation on LD-TD plane. Consequently, the heterogeneous deformation is well characterised by surface observation on LD-TD plane. Each specimen is denoted as SCXX, where XX indicates the angle ϕ . To examine the effect of the pre-strain on the deformation behaviour, we also fabricated specimens using the pre-deformed DS crystal with dimensions of $5 \times 5 \times 10\text{ mm}^3$, which was deformed up to a strain of 9% by compression along the crystal growth direction. The pre-strained specimens are

denoted as PSXX, where XX indicates the angle ϕ .

Micro-tensile tests were performed under ambient laboratory conditions at a nominal strain rate of $2.0 \times 10^{-3} \text{ s}^{-1}$. Figure 2c shows a schematic illustration of micro-tensile testing machine. Using glue, both ends of the specimen, which were more than 0.5 mm away from the gauge section, were attached to the specimen holder and the jig connected to the load cell (Fig. 2d). A piezoelectric actuator with a position accuracy of 10 nm was used for displacement control. The load was measured using a load cell with a capacity of 2 N or 200 mN. The strain was continuously measured via optical microscope imaging of the gauge section of the specimen during each tensile test. Some specimens having a hole at the one end were loaded using a 200 μm diameter pin, as shown in Fig. 2e. The specimens were unloaded immediately after the onset of yielding to fabricate a foil sample for transmission electron microscopy (TEM) using FIB. The TEM observations were performed with a JEOL JEM-2100PLUS transmission electron microscope operated at an accelerating voltage of 200 kV.

3. Experimental results

3.1 Deformation behaviour of as-solidified single crystals

Figure 3 shows the stress–strain curves of tensile loading tests for the specimens SC14 and SC60. The stress–strain curve for SC14—indicated by open symbols—exhibited well-defined yielding at a peak stress of $\sigma \approx 165 \text{ MPa}$, which was followed by a steep decrease in the flow stress. After several steep increases and decreases in the flow stress, the stress gradually increased to $\sigma \approx 100 \text{ MPa}$ at $\varepsilon \approx 56\%$, followed by a steep decrease in the stress until the final failure at $\varepsilon \approx 70\%$. On the other hand, the stress–strain response for the SC60 specimen—indicated by solid symbols—showed a steep decrease in the stress after the peak stress $\sigma \approx 55 \text{ MPa}$ at $\varepsilon \approx 1\%$; the flow–stress level immediately before unloading was $\sim 30 \text{ MPa}$. Because of the abrupt change in the force and displacement, no data were recorded from yielding to the point just before unloading. The stress-strain curves for SC30 and SC70 specimens are also shown in Supplementary Note.

3.2 Evaluation of deformation bands in deformed single-crystalline specimens

The deformation microstructures of the SC14 and SC60 specimens were examined using optical and electron microscopy. The observations indicated significantly

different types of deformation bands depending on the angle ϕ : a kink band for the SC14 specimen and a slip band for the SC60 specimen, which were characterised as follows:

(i) Kink band in deformed SC14 specimen

Figure 4a shows an optical micrograph of the SC14 specimen at $\varepsilon = 6.4\%$, immediately after the steep decrease in the flow stress, where a deformation band was formed, as indicated by the white solid lines. A schematic illustration of this deformation band is shown in Fig. 4b; the angle between the LD and the interface of the band region, which is coloured by dark grey, was $\sim 33^\circ$. This angle suggests that the deformation band in the deformed SC14 is a kink band formed by the localisation of deformation whose slip direction is nearly perpendicular to the interface of the band region, as previously reported [44, 45]. Subsequently, several kink bands were formed in the vicinity of the first kink band during steep decrease in the flow stress (Supplementary Video). The optical micrographs of the SC14 specimen at $\varepsilon = 17\%$ and 57% in Figs. 4c and d indicate that the kink band grew into the outer region of the specimen. As shown in Supplementary Note, the deformed SC30 specimen also shows kink banding.

Figure 4e displays the TEM bright-field (BF) image obtained from the deformed SC14 specimen after failure, together with selected-area electron diffraction (SAED) patterns taken with the electron beam (EB) direction parallel to $[1\bar{1}00]$ at the matrix (Fig. 4f) and the deformation band (Fig. 4g). These diffraction patterns indicate that the orientation relationship between the points “F” and “G” in Fig. 4e was a rotation of 40° – 45° about $[1\bar{1}00]$. That is, the angle between the normal directions of the basal plane for these points was 40° – 45° . The TEM observation also indicates several kink regions including rotational kink regions [13], where the basal plane is gradually bent.

(ii) Slip band in deformed SC60 specimen

Figure 5a shows a scanning electron microscopy (SEM) image of the SC60 specimen at $\varepsilon = 14\%$. The strain was localised in the shape of a band whose interfaces are nearly parallel to the basal plane, as schematically shown in Fig. 5b. This suggests that the deformation band corresponds to a slip band [44, 45]. The SEM image after failure for the SC70 specimen in Supplementary Note also indicates a formation of slip band parallel to the basal plane.

Figure 5c shows a TEM BF image together with SAED patterns taken with the EB direction parallel to [0001] for the band in the SC60 specimen. The TEM BF image revealed the formation of a basal dislocation network on the (0001) plane within the slip band. Sharp et al. reported that the basal dislocation network is constructed by interaction between basal slip systems with two or more distinct $\langle 11\bar{2}0 \rangle$ Burgers vectors in pure Mg deformed at a low temperature [46]. These findings suggest that basal slips with different $\langle 11\bar{2}0 \rangle$ Burgers vectors were activated during basal slip banding, whereas a single slip of the basal slip system was expected according to the initial crystal orientation, as shown in the inverse pole figure of Fig. 3.

3.3 Influence of pre-strain on deformation behaviour

The influence of the pre-strain on the deformation behaviour was examined. In Fig. 6, comparisons between the as-solidified and pre-strained specimens are shown. The pre-strained specimens were compressed with a strain of 9% along the solidification direction, as explained in Section 2.

The stress–strain behaviour of the PS14 specimen denoted by solid symbols in Fig. 6a is qualitatively similar to that of SC14, as shown in Fig. 3. That is, the stress–strain curves exhibited steep increases and decreases in the flow stress after well-defined yielding, which was followed by a gradual increase in the flow stress up to failure. In the deformed PS14 specimen, a kink-type deformation band, which was similar to the kink band for SC14 in Fig. 4, was formed. However, the stress levels of yielding and the subsequent flow stress were clearly lower for PS14 than for SC14.

The stress–strain response for the SC45 specimen denoted by open symbols in Fig. 6b showed a steep decrease in stress after the peak stress $\sigma \approx 60$ MPa, followed by a gradual decrease in the flow stress. In contrast, the stress–strain curve of the PS45 specimen, which is denoted by solid symbols in Fig. 6b, exhibited a continuous elastic–plastic transition. It does not show clear yielding and a steep decrease in the flow stress. The non-linear deformation was started at ~ 30 MPa, which is significantly lower than the peak stress of ~ 60 MPa in the SC45 specimen.

In the SC45 specimen at $\varepsilon = 2.4\%$ in Fig. 6c, a deformation band parallel to the basal plane, which corresponds to a slip band, was formed; there were no other noticeable slip traces. There was a crack at the slip band boundary, as indicated by an arrow in Fig. 6c, which could lead to premature fracture. The deformed PS45 specimen

at $\varepsilon = 7.2\%$ in Fig. 6d showed a thicker slip band, which probably contributed to continuous plastic flow at a nearly constant stress level in Fig. 6b. Comparison between the deformation behaviour of SC45 and PS45 suggests that pre-strain effectively eliminated pronounced yielding with a steep decrease in the flow stress. These results agree with the micro-compression study of the pre-strained Mo alloy conducted by Bei et al. [47]. They indicated that the increase of the initial dislocation density is responsible for the decreasing flow stress of the pre-strained microcrystals, which is contrary to bulk-crystal behaviour.

3.4 Estimated critical resolved shear stress (CRSS) for basal slip system

Table 1 shows previously reported CRSS values for a basal slip system [7, 16, 41, 48–50], as well as the values obtained in this study. The present CRSSs for basal slip system were estimated by using the peak stress just before steep decrease in stress except for the P45 specimen where gradual elastic-plastic transition was observed. For the P45 specimen, therefore, 0.2% offset stress was used for the estimation of the CRSS. The values were significantly varied in the range of 10–30 MPa depending on the reports. The values obtained in this study for SC45, SC60, and SC70 were 25–30 MPa. These are comparable to the CRSS of 27–30 MPa at a formation of the basal slip band accompanied by a steep load decrease, which was measured via a micro-bending test of an 18R-type LPSO-phase single crystal [49]. On the other hand, the CRSS obtained for the pre-strained PS45 specimen, which was determined to be 15 MPa, corresponds to a resolved shear stress (RSS) of 12–19 MPa for a lower yield point after the slip banding in the specimens without pre-strain. These values are close to the CRSS (9.4 MPa) reported for the basal slip obtained from a $[\bar{7}1141]$ loaded single-crystalline specimen [41], which exhibited continuous plastic flow without distinct yielding phenomena, similar to the stress–strain response of the PS45 specimen.

In Fig. 7, the RSS values for the basal slip system are plotted with respect to the angle between the loading axis and the $[0001]$ direction, ϕ . For the SC14 and SC45 specimens, the tensile tests were performed twice, and the CRSS values obtained from the repeated tests are very close as shown in Fig. 7. The small variations for each specimen indicate a reasonable repeatability of the present tensile test. The LPSO-phase single crystal subjected to tensile loading shows basal plane orientation

dependence of the CRSS value, which tends to increase gradually with the decrease of ϕ , regardless of the existence of the pre-strain. Several studies reported that the CRSS value for basal slip in HCP metals decreases with the increase of the stress component normal to the basal plane in Zn single crystals, according to a biaxial loading test [51] and an atomistic simulation study of Mg [52, 53]. In Fig. 7, a smaller ϕ yields a higher stress normal to the slip plane. Therefore, the present experimental results showed that the LPSO-phase single crystals exhibited the opposite trend to the literature, where a higher normal stress led to a higher CRSS.

4. Discussion

In the previous sections, single crystals of an $\text{Mg}_{85}\text{Zn}_6\text{Y}_9$ alloy with the 18R-LPSO phase under tensile loading exhibited non-uniform deformation accompanied by slip or kink band formation depending on the crystal orientation relative to the LD. Among them, SC14 exhibited pronounced ductility, where kink bands were formed and grown, as shown in Fig. 4. To examine the underlying mechanism of the deformation behaviour and the kink banding, crystal plasticity finite element analysis was performed.

4.1 Numerical procedures

4.1.1 Crystal plasticity finite element method

In this study, we used a finite element method with a rate-dependent crystal plasticity constitutive model, which was proposed by Peirce et al. [54]. In the constitutive model, the shear strain rate $\dot{\gamma}^{(\alpha)}$ of the slip system α was calculated as follows:

$$\dot{\gamma}^{(\alpha)} = \dot{\gamma}_0 \operatorname{sgn}(\tau^{(\alpha)}) \left| \frac{\tau^{(\alpha)}}{g^{(\alpha)}} \right|^{1/m}, \quad (1)$$

where $\tau^{(\alpha)}$, m , and $\dot{\gamma}_0$ are the RSS for slip system α , the strain rate sensitivity exponent, and the reference shear strain rate, respectively. For the present calculation, $m = 0.02$ and $\dot{\gamma}_0 = 0.001$ were employed. The following Voce-type hardening law for $g^{(\alpha)}$ in Eq. (1) was assumed as follows:

$$g^{(\alpha)} = \tau_0^{(\alpha)} + \left(\tau_1^{(\alpha)} + \theta_1^{(\alpha)} \Gamma^{(\alpha)} \right) \left\{ 1 - \exp \left(- \frac{\theta_0^{(\alpha)} \Gamma^{(\alpha)}}{\tau_1^{(\alpha)}} \right) \right\}. \quad (2)$$

In Eq. (2), $I^{(\alpha)}$ is the accumulated slip for slip system α . Only the basal slip system was considered as a possible slip system in the LPSO structure, because the dominant activity of the basal slip system at room temperature was previously reported [7, 55]. The specific values of the material parameters in Eq. (2) are shown in Table 2, which were identified via fitting to the experimental stress–strain curve of SC14 in Fig. 3a. Eventually, the hardening law with the parameters in Table 2 describes near-linear hardening, which is frequently assumed for basal slip system in Mg and Mg alloys. The anisotropic elastic constants for 18R-LPSO reported by Tane et al. [56] were used.

4.1.2 Analysis model and boundary conditions

Figure 8 shows a schematic diagram of the geometry and boundary conditions for the present analysis, which are based on the experimental specimen and the loading condition in the present micro-tensile tests. The model was divided into 6,400 finite elements with a 20-node solid element, as shown in Fig. 8; the bottom surface was fixed in the LD, while tensile loading was applied on the top surface in the LD with displacement control. For the tensile loading, the displacement perpendicular to the LD was not fixed. The initial crystal orientations were given by the Euler angles, which were obtained via EBSD analysis for SC14.

4.2 Kink band formation and growth mechanism under tensile loading

4.2.1 Numerically reproduced deformation behaviour

The open symbols in Fig. 9 show the calculated stress–strain curves of the SC14 model; the experimental stress–strain curve in the figure is indicated by a solid line for comparison. The calculated result shows a sudden decrease in the flow stress at $\varepsilon = \sim 4.2\%$ after a plateau stress region, which is followed by a gradual decrease in the flow stress. The overall flow-stress level is very close to the experimental result, whereas a detailed comparison of the stress–strain curves between the experiment and calculation is difficult especially in the early stage of deformation because of the lack of experimental data points.

In Fig. 9, calculated distributions of the accumulated basal slip at $\varepsilon = 3.0, 6.0, 10$ and 50% are indicated. From $\varepsilon = 3.0\%$ to 6.0% , the basal slip is locally accumulated near the middle of the specimen. At $\varepsilon = 6.0\%$, a slip-localised region with a band-like shape is formed where the interface between the slip-localised region and the surrounding region is nearly perpendicular to basal plane. Subsequently, from $\varepsilon = 10\%$

to 50%, the slip-localised region is expanded to the surrounding region. This development of accumulation of the basal slip is qualitatively similar to the experimental observation shown in Figs. 4a–d.

As shown above, both stress–strain behaviour and localised deformation of the SC14 are well reproduced by the present crystal plasticity analysis. Therefore, in what follows, the underlying deformation mechanism of the nonuniform deformation is discussed on the basis of the present numerically reproduced results.

4.2.2 Kink band formation mechanism

The slip localisation at the early stage of deformation is discussed. In Fig. 10a, the solid symbols show a calculated development of ϕ in the middle of the specimen. In Fig. 10a, the stress–strain curve is also indicated by a grey broken line. After gradually decreasing up to $\varepsilon = \sim 4.3\%$, ϕ steeply increases from $\varepsilon = \sim 4.3\%$ where the flow stress shows a sudden decrease. Figures 10b and c show distributions of ϕ before ($\varepsilon = 3.0\%$) and after ($\varepsilon = 6.0\%$) the sudden stress decrease, respectively. At $\varepsilon = 6.0\%$, a band-like region with significant intragranular misorientations is developed in the middle of the specimen. This band-like region in Fig. 10c is similar to that of the slip-localised region in Fig. 9, which suggests that the significant intragranular misorientation was developed by lattice rotation owing to the accumulation of the basal slip. The open symbols in Fig. 10d show a calculated development of the Schmid factor for the basal slip in the middle of the specimen, where the stress–strain curve is also indicated by a grey broken line. The Schmid factor steeply increases from $\varepsilon = \sim 4.3\%$, similar to ϕ in Fig. 10a. This steep increase in the Schmid factor leads to a sudden decrease in the nominal stress because the increase in the Schmid factor decreases the resolved shear stress for the slip system. This mechanism of softening is referred to as “geometrical softening.”

The morphological features—basal slip accumulation in the form of a band-like shape whose interfaces are nearly perpendicular to the active slip plane and a significant development of intragranular misorientation within the band-like region—correspond to the typical features of the kink–mode deformation band [44, 45]. The steep decrease in the stress caused by geometrical softening is similar to the compressive loading behaviour with kink band formation discussed in previous studies [22, 23]. Therefore, we conclude that slip localisation and significant lattice rotation during tensile deformation of SC14 correspond to kink band formation, where

geometrical softening promotes the development. Notably, the initial crystal orientation preferable for kink band formation is different between tension and compression. In tension, ϕ should be smaller for a pronounced geometrical softening, whereas it should be larger in compression, as discussed in a previous report [22].

4.2.3 Growth mechanism of the kink band

The distributions of the accumulated basal slip in Fig. 9 exhibit a significant expansion of the strain-localised region from $\varepsilon = 10\%$ to 50% , which qualitatively corresponds to the experimental observation in Figs. 4c and d. In this section, the mechanism underlying the growth of the kink band during tensile loading is discussed.

Figures 11a, b, and c show the calculated distributions of ϕ at $\varepsilon = 10\%$, 20% , and 50% , respectively. Figures 11d, e, and f show the line profiles of ϕ from the point “0” to the point “1” on the specimen, as shown in Figs. 11a, b, and c, respectively. Whereas the maximum angle ϕ gradually increases, it does not exceed 65° even at $\varepsilon = 50\%$. This means that the activity of the basal slip system is suppressed when the angle reaches $\sim 65^\circ$ because the change in ϕ is primarily due to the lattice rotation by the activity of the basal slip system. Importantly, as shown in Figs. 11d, e, and f, the region where ϕ increases shifts to the outer region of the specimen, which corresponds to the growth of the kink band.

The distributions of the Schmid factor for the basal slip system at $\varepsilon = 10\%$, 20% , and 50% are shown in Figs. 12a, b, and c, respectively. Figures 12d, e, and f show the line profiles of the Schmid factor along the point “0” to the point “1” on the specimen, as shown in Figs. 12a, b, and c. Whereas the region near the middle of the specimen shows a maximum Schmid factor of 0.5 at $\varepsilon = 10\%$, the outer regions have the maximum Schmid factor 0.5 at $\varepsilon = 20\%$ and 50% . Notably, in the middle of the specimen, the Schmid factor decreases from $\varepsilon = 10\%$ to 50% , which is due to the lattice rotation up to larger angles more than 45° , as shown in Fig. 11. Consequently, the activity of the basal slip system near the middle of the specimen decreases, which results in the expansion of the slip localised region into the outer region, as shown in Fig. 9. In other words, the growth of the kink band is caused by the change in the Schmid factor by lattice rotation.

The process of kink band growth would suppress early localised failure because the strain localised region propagates to the neighbouring region. As a result, an extended ductility over 50% was achieved during deformation accompanied by kink band

formation even in the LPSO structure with a strong plastic anisotropy. In other words, the strong plastic anisotropy and kink-mode strain localisation does not necessarily lead to a brittle failure. However, in bulk polycrystals, localised formation of kink bands induces frequent initiation of microcracks at grain boundaries [16], which is probably due to plastic incompatibility near the grain boundaries [57]. Therefore, in order to accommodate heterogeneous deformation owing to the plastic incompatibility, α -Mg phase with relatively less anisotropic plasticity is crucially important to achieve reasonable ductility of bulk two phase LPSO-type Mg alloys such as $\text{Mg}_{97}\text{Zn}_1\text{Y}_2$ consisted of LPSO phase and α -Mg phase [9]. In future works, interactions of slip activities at phase interfaces between LPSO phase and α -Mg phase should be investigated to gain understandings of microscopic mechanism of ductility in high strength LPSO-type Mg alloys.

5. Conclusions

The deformation behaviour in a single-crystal LPSO structure under tensile loading was investigated via micro-tensile tests and crystal plasticity finite element analysis. Depending on the loading direction relative to the crystal orientations, a kink or slip band was formed in the deformed single crystals, which was successfully reproduced by the numerical calculation. According to microstructural observations and the calculated activity of the deformation modes, the mechanism underlying the formation of the deformation band was discussed. Consequently, the following conclusions were drawn.

- (1) Micro-tensile tests indicated that a kink band was formed in specimens for which the angle between the [0001] direction and the loading direction was 14° and 30° . In contrast, in specimens for which the angle was 45° , 60° , and 70° deformation was accompanied by the formation of a slip band.
- (2) The as-solidified and pre-strained specimens that showed the formation of a slip band exhibited significantly different deformation behaviour. The as-solidified specimen exhibited well-defined yielding and subsequent steep softening whereas the pre-strained specimen showed a continuous elastic-plastic transition. In contrast, the as-solidified and pre-strained specimens that showed the formation of a kink band exhibited qualitatively similar stress-strain behaviour.
- (3) The crystal plasticity finite element analysis, where only the basal slip system was

implemented as a possible deformation mode, successfully reproduced the kink band formation and the subsequent growth during tensile loading of the single-crystal LPSO structure.

- (4) The kink band was formed by the accumulation of basal slip, which is enhanced by geometrical softening owing to the lattice rotation. Subsequently, the activity of the basal slip system was suppressed owing to further lattice rotation because the Schmid factor for the basal slip system decreased. Consequently, the kink band grew into the outer region of the specimen, where the Schmid factor was the highest.

Acknowledgment

This study was partially supported by JSPS KAKENHI for Scientific Research on Innovative Areas “MFS Materials Science (Grant numbers 18H05480 and 19H05133)” and JSPS KAKENHI Grant numbers JP18H01339. This work was also performed under the Iketani Science and Technology Foundation (No. 0301035-A).

References

- [1] Y. Kawamura, K. Hayashi, A. Inoue, T. Masumoto, Rapidly solidified powder metallurgy $\text{Mg}_{97}\text{Zn}_1\text{Y}_2$ alloys with excellent tensile yield strength above 600 MPa, *Mater. Trans.* 42 (2001) 1172–1176. <https://doi.org/10.2320/matertrans.42.1172>
- [2] E. Abe, A. Ono, T. Itoi, M. Yamasaki, Y. Kawamura, Polytypes of long-period stacking structures synchronized with chemical order in a dilute Mg-Zn-Y alloy, *Philos. Mag. Lett.* 9 (2011) 690–696. <https://doi.org/10.1080/09500839.2011.609149>
- [3] D. Egusa, E. Abe, The structure of long period stacking/order Mg-Zn-RE phases with extended non-stoichiometry ranges, *Acta Mater.* 60 (2012) 166–178. <https://doi.org/10.1016/j.actamat.2011.09.030>
- [4] K. Kishida, K. Nagai, A. Matsumoto, A. Yasuhara, H. Inui, Crystal structures of highly-ordered long-period stacking-ordered phases with 18R, 14H and 10H-type stacking sequences in the Mg-Zn-Y system, *Acta Mater.* 99 (2015) 228–239. <https://doi.org/10.1016/j.actamat.2015.08.004>
- [5] T. Itoi, T. Seimiya, Y. Kawamura, M. Hirohashi, Long period stacking structures observed in $\text{Mg}_{97}\text{Zn}_1\text{Y}_2$ alloy, *Scr. Mater.* 51 (2004) 107–111. <https://doi.org/10.1016/j.scriptamat.2004.04.003>

- [6] Y. Chino, M. Mabuchi, S. Hagiwara, H. Iwasaki, A. Yamamoto, H. Tsubakino, Novel equilibrium two phase Mg alloy with the long-period ordered structure, *Scr. Mater.* 51 (2004) 711–714. <https://doi.org/10.1016/j.scriptamat.2004.06.007>
- [7] K. Hagihara, N. Yokotani, Y. Umakoshi, Plastic deformation behavior of Mg₁₂YZn with 18R long-period stacking ordered structure, *Intermetallics* 18 (2010) 267–276. <https://doi.org/10.1016/j.intermet.2009.07.014>
- [8] X.H. Shao, Z.Q. Yang, X.L. Ma, Strengthening and toughening mechanisms in Mg-Zn-Y alloy with a long period stacking ordered structure, *Acta Mater.* 58 (2010) 4760–4771. <https://doi.org/10.1016/j.actamat.2010.05.012>
- [9] M. Yamasaki, K. Hashimoto, K. Hagihara, Y. Kawamura, Effect of multimodal microstructure evolution on mechanical properties of Mg-Zn-Y extruded alloy, *Acta Mater.* 59 (2011) 3646–3658. <https://doi.org/10.1016/j.actamat.2011.02.038>
- [10] K. Hagihara, Y. Sugino, Y. Fukusumi, Y. Umakoshi, T. Nakano, Plastic deformation behavior of Mg₁₂ZnY LPSO-phase with 14H-typed structure, *Mater. Trans.* 52 (2011) 1096–1103. <https://doi.org/10.2320/matertrans.MC201007>
- [11] K. Hiraga, A. Yasuhara, K. Saito, Dislocations in deformation microstructure of extruded Mg₉₇Y₂Zn₁ alloy studied by high-angle annular detector dark-field scanning transmission electron microscopy (HAADF-STEM), *Mater. Trans.* 53 (2012) 1385–1390. <https://doi.org/10.2320/matertrans.M2012115>
- [12] H. Gao, K. Ikeda, T. Morikawa, K. Higashida, H. Nakashima, Microstructures of long-period stacking ordered phase of Mg-Zn-Y alloy, *Mater. Trans.* 54 (2013) 632–635. <https://doi.org/10.2320/matertrans.MI201219>
- [13] D. Egusa, M. Yamasaki, Y. Kawamura, E. Abe, Micro-kinking of the long-period stacking/order (LPSO) phase in a hot-extruded Mg₉₇Zn₁Y₂ alloy, *Mater. Trans.* 54 (2013) 698–702. <https://doi.org/10.2320/matertrans.MI201216>
- [14] M. Yamasaki, K. Hagihara, S. Inoue, J.P. Hadorn, Y. Kawamura, Crystallographic classification of kink bands in an extruded Mg-Zn-Y alloy using intragranular misorientation axis analysis, *Acta Mater.* 61 (2013) 2065–2076. <https://doi.org/10.1016/j.actamat.2012.12.026>
- [15] J.K. Kim, S. Sandlöbes, D. Raabe, On the room temperature deformation mechanisms of a Mg-Y-Zn alloy with long-period-stacking-ordered structures, *Acta Mater.* 82 (2015) 414–423. <https://doi.org/10.1016/j.actamat.2014.09.036>
- [16] K. Hagihara, T. Okamoto, H. Izuno, M. Yamasaki, M. Matsushita, T. Nakano, Y.

- Kawamura, Plastic deformation behavior of 10H-type synchronized LPSO phase in a Mg-Zn-Y system, *Acta Mater.* 109 (2016) 90–102. <https://doi.org/10.1016/j.actamat.2016.02.037>
- [17] X.H. Shao, Z.Z. Peng, Q.Q. Jin, X.L. Ma, Atomic-scale segregations at the deformation-induced symmetrical boundary in an Mg-Zn-Y alloy, *Acta Mater.* 118 (2016) 177–186. <https://doi.org/10.1016/j.actamat.2016.07.054>
- [18] T. Matsumoto, M. Yamasaki, K. Hagihara, Y. Kawamura, Configuration of dislocations in low-angle kink boundaries formed in a single crystalline long-period stacking ordered Mg-Zn-Y alloy, *Acta Mater.* 151 (2018) 112–124. <https://doi.org/10.1016/j.actamat.2018.03.034>
- [19] K. Hagihara, Z. Li, M. Yamasaki, Y. Kawamura, T. Nakano, Strengthening mechanisms acting in extruded Mg-based long-period stacking ordered (LPSO)-phase alloys, *Acta Mater.* 163 (2019) 226–239. <https://doi.org/10.1016/j.actamat.2018.10.016>
- [20] R. Matsumoto, M. Uranagase, N. Miyazaki, Molecular dynamics analyses of deformation behavior of long-period-stacking-ordered structures, *Mater. Trans.* 54 (2013) 686–692. <https://doi.org/10.2320/matertrans.MI201211>
- [21] R. Matsumoto, M. Uranagase, Deformation analysis of the long-period stacking-ordered phase by using molecular dynamics simulations: Kink deformation under compression and kink boundary migration under tensile strain, *Mater. Trans.* 56 (2015) 957–962. <https://doi.org/10.2320/matertrans.MH201408>
- [22] T. Mayama, T. Ohashi, Y. Tadano, K. Hagihara, Crystal plasticity analysis of development of intragranular misorientations due to kinking in hcp single crystals subjected to uniaxial compressive loading, *Mater. Trans.* 56 (2015) 963–972. <https://doi.org/10.2320/matertrans.MH201403>
- [23] K. Hagihara, T. Mayama, M. Honnami, M. Yamasaki, H. Izuno, T. Okamoto, T. Ohashi, T. Nakano, Y. Kawamura, Orientation dependence of the deformation kink band formation behavior in Zn single crystal, *Int. J. Plasticity* 77 (2016) 174–191. <https://doi.org/10.1016/j.ijplas.2015.10.005>
- [24] E. Orowan, A type of plastic deformation new in metals, *Nature* 149 (1942) 643–644. <https://doi.org/10.1038/149643a0>
- [25] J.B. Hess, C.S. Barrett, Structure and nature of kink bands in zinc, *Trans. Metall. AIME* 185 (1949) 599–606. <https://doi.org/10.1007/BF03398902>
- [26] D.C. Jillson, An experimental survey of deformation and annealing processes in

- zinc, Trans. Metall. AIME 188 (1950) 1009–1018.
<https://doi.org/10.1007/BF03399099>
- [27] F.C. Frank, A.N. Stroh, On the theory of kinking, Proceedings of the Physical Society. Section B, 65 (1952) 811–821. <https://doi.org/10.1088/0370-1301/65/10/311>
- [28] A. G. Evans, W. F. Adler, Kinking as a mode of structural degradation in carbon fiber composites, Acta Metallurgica 26 (1978) 725–738.
[https://doi.org/10.1016/0001-6160\(78\)90023-8](https://doi.org/10.1016/0001-6160(78)90023-8)
- [29] M. W. Barsoum, A. Murugaiah, S. R. Kalidindi, T. Zhen, Y. Gogotsi, Kink bands, nonlinear elasticity and nanoindentations in graphite, Carbon 42 (2004) 1435–1445.
<https://doi.org/10.1016/j.carbon.2003.12.090>
- [30] J. C. W. Lo, Y. C. Lu, D. M. Shinozaki, Kink band formation during micro-indentation of oriented polypropylene, Mater. Sci. Eng. A 409 (2005) 76–86.
<https://doi.org/10.1016/j.msea.2005.05.112>
- [31] A. G. Zhou, S. Basu, M. W. Barsoum, Kinking nonlinear elasticity, damping and microyielding of hexagonal close-packed metals, Acta Mater. 56 (2008) 60–67.
<https://doi.org/10.1016/j.actamat.2007.08.050>
- [32] L. Benabou, Finite strain analysis of wood species under compressive failure due to kinking, Int. J. Solids Struct. 49 (2012) 408–419.
<https://doi.org/10.1016/j.ijsolstr.2011.09.024>
- [33] J. Washburn, E. R. Parker, Kinking in Zinc single-crystal tension specimens, Trans. AIME J. Metals 4 (1952) 1076–1078. <https://doi.org/10.1007/BF03397774>
- [34] J. J. Gilman, T. A. Read, Bend plane phenomena in the deformation of Zinc monocrystals, Trans. AIME J. Metals 5 (1953) 49–55.
<https://doi.org/10.1007/BF03397447>
- [35] A. M. Gervais, J. T. Norton, N. J. Grant, Kink band formation in high purity aluminum during creep at high temperatures, Trans. AIME (1953) 1487–1492.
- [36] K. C. A. Blasdale, R. King, Tensile kinking in single crystals of Cadmium, Phys. Stat. Sol. 10 (1965) 175–184. <https://doi.org/10.1002/pssb.19650100117>
- [37] A. S. Keh, Work hardening and deformation sub-structure in iron single crystals deformed in tension at 298°K, Philos. Mag. 12 (1965) 9–30.
<https://doi.org/10.1080/14786436508224942>
- [38] M. W. Kapp, A. Hohenwarter, S. Wurster, B. Yang, R. Pippan, Anisotropic deformation characteristics of an ultrafine- and nanolamellar pearlitic steel, Acta Mater.

- 106 (2016) 239–248. <https://doi.org/10.1016/j.actamat.2015.12.037>
- [39] T. Nizolek, N. A. Mara, I. J. Beyerlein, J. T. Avallone, T. M. Pollock, Enhanced plasticity via kinking in cubic metallic nanolaminates, *Adv. Eng. Mater.* 17 (2015) 781–785. <https://doi.org/10.1002/adem.201400324>
- [40] T. J. Nizolek, M. R. Begley, R. J. McCabe, J. T. Avallone, N. A. Mara, I. J. Beyerlein, T. M. Pollock, Strain fields induced by kink band propagation in Cu-Nb nanolaminate composites, *Acta Mater.* 133 (2017) 303–315. <https://doi.org/10.1016/j.actamat.2017.04.050>
- [41] Y. Mine, R. Maezono, H. Oda, M. Yamasaki, Y. Kawamura, K. Takashima, Deformation behavior of long-period stacking ordered structured single crystals in $\text{Mg}_{85}\text{Zn}_6\text{Y}_9$ alloy, *Mater. Trans.* 56 (2015) 952–956. <https://doi.org/10.2320/matertrans.MH201415>
- [42] Y. Mine, K. Koga, O. Kraft, K. Takashima, Mechanical characterisation of hydrogen-induced quasi-cleavage in a metastable austenitic steel using micro-tensile testing, *Scr. Mater.* 113 (2016) 176–179. <https://doi.org/10.1016/j.scriptamat.2015.11.013>
- [43] Y. Mine, S. Nakamichi, K. Koga, K. Takashima, O. Kraft, Deformation behaviour of nano-twinned single crystals of an Fe–19Cr–16Ni austenitic alloy, *Mater. Sci. Eng. A* 675 (2016) 181–191. <https://doi.org/10.1016/j.msea.2016.08.059>
- [44] R. J. Asaro, J. R. Rice, Strain localization in ductile single crystals, *J. Mech. Phys. Solids* 25 (1977) 309–338. [https://doi.org/10.1016/0022-5096\(77\)90001-1](https://doi.org/10.1016/0022-5096(77)90001-1)
- [45] S. Forest, Modeling slip, kink and shear banding in classical and generalized single crystal plasticity, *Acta Mater.* 46 (1998) 3265–3281. [https://doi.org/10.1016/S1359-6454\(98\)00012-3](https://doi.org/10.1016/S1359-6454(98)00012-3)
- [46] J.V. Sharp, M.J. Makin, J.W. Christian, Dislocation structure in deformed single crystals of magnesium, *Phys. Stat. Sol.* 11 (1965) 845–864. <https://doi.org/10.1002/pssb.19650110235>
- [47] H. Bei, S. Shim, G.M. Pharr, E.P. George, Effects of pre-strain on the compressive stress–strain response of Mo-alloy single-crystal micropillars, *Acta Mater.* 56 (2008) 4762–4770. <https://doi.org/10.1016/j.actamat.2008.05.030>
- [48] A. Inoue, K. Kishida, H. Inui, K. Hagihara, Compression of micro-pillars of a long period stacking ordered phase in the Mg-Zn-Y system, *Mater. Res. Soc. Symp. Proc.* 1516 (2013) 151–156. <https://doi.org/10.1557/opl.2012.1749>

- [49] Y. Mine, R. Maezono, T. Mayama, J. Wu, Y. L. Chiu, P. Bowen, K. Takashima, Plasticity and crack extension in single-crystalline long-period stacking ordered structures of $\text{Mg}_{85}\text{Zn}_6\text{Y}_9$ alloy under micro-bending, *J. Alloys Compd.* 718 (2017) 433–442. <https://doi.org/10.1016/j.jallcom.2017.05.192>
- [50] R. Chen, S. Sandlöbes, C. Zehnder, X. Zeng, S. Korte-Kerzel, D. Raabe, Deformation mechanisms, activated slip systems and critical resolved shear stresses in an Mg-LPSO alloy studied by micro-pillar compression, *Mater. Des.* 154 (2018) 203–216. <https://doi.org/10.1016/j.matdes.2018.05.037>
- [51] J.A. Barendrecht, W.N. Sharpe Jr., The effect of biaxial loading on the critical resolved shear stress of zinc single crystals, *J. Mech. Phys. Solids* 21 (1973) 113–123. [https://doi.org/10.1016/0022-5096\(73\)90033-1](https://doi.org/10.1016/0022-5096(73)90033-1)
- [52] C.D. Barrett, H.E. Kadiri, M.A. Tschopp, Breakdown of the Schmid law in homogeneous and heterogeneous nucleation events of slip and twinning in magnesium, *J. Mech. Phys. Solids* 60 (2012) 2084–2099. <https://doi.org/10.1016/j.jmps.2012.06.015>
- [53] M. Uranagase, R. Matsumoto, Effects of normal stresses on the homogeneous nucleation of a basal dislocation in magnesium, *Comput. Mater. Sci.* 113 (2016) 143–147. <https://doi.org/10.1016/j.commatsci.2015.11.031>
- [54] D. Peirce, R. J. Asaro, A. Needleman, Material rate dependence and localized deformation in crystalline solids, *Acta Metall.* 31 (1983) 1951–1976. [https://doi.org/10.1016/0001-6160\(83\)90014-7](https://doi.org/10.1016/0001-6160(83)90014-7)
- [55] K. Hagihara, Y. Fukusumi, M. Yamasaki, T. Nakano, Y. Kawamura, Non-basal slip systems operative in Mg_{12}ZnY long-period stacking ordered (LPSO) phase with 18R and 14H structures, *Mater. Trans.* 54 (2013) 693–697. <https://doi.org/10.2320/matertrans.MI201208>
- [56] M. Tane, Y. Nagai, H. Kimizuka, K. Hagihara, Y. Kawamura, Elastic properties of an Mg-Zn-Y alloy single crystal with a long-period stacking-ordered structure, *Acta Mater.* 61 (2013) 6338–6351. <https://doi.org/10.1016/j.actamat.2013.06.041>
- [57] R.E. Hook, J.P. Hirth, The deformation behavior of isoaxial bicrystals of Fe–3%Si, *Acta Metall.* 15 (1967) 535–551. [https://doi.org/10.1016/0001-6160\(67\)90087-9](https://doi.org/10.1016/0001-6160(67)90087-9)

Figure captions

Figure 1 Schematic illustration of a 18R-type LPSO structure in Mg-Zn-Y alloy.

Figure 2 (a) SEM back scattered electron image of the microstructure of the $\text{Mg}_{85}\text{Zn}_6\text{Y}_9$ alloy. (b) Geometry of micrometer-sized tensile specimen. (c) Schematic illustration of micro-tensile testing machine. The thin specimens were held by (d) gluing both ends or (e) pin with diameter of 200 μm .

Figure 3 Stress–strain curves for the SC14 and SC60 specimens. The tensile test of SC60 specimen was interrupted just after yielding and unloaded to stress of zero.

Figure 4 (a) Optical micrograph of sample surface of SC14 specimen at $\varepsilon = 6.4\%$ and (b) the corresponding schematic illustration of the kink band. (c) and (d) optical micrographs of SC14 at $\varepsilon = 17\%$ and $\varepsilon = 57\%$, respectively. (e) BF TEM image of the deformed microstructure of the SC14 specimen after failure (beam axis $\sim [1\bar{1}00]$), and (f, g) SAED pattern in matrix and kink deformation band, respectively.

Figure 5 (a) SEM image of the SC60 specimen interrupted just after formation of slip band at $\varepsilon = 14\%$ and (b) corresponding schematic illustration of slip band. (c) BF TEM image of the dislocation structure within the slip band of SC60 specimen (beam axis $\sim [0001]$).

Figure 6 Stress–strain curves for the (a) SC14 and pre-strained PS14, and (b) SC45 and pre-strained PS45 specimens. Optical micrographs showing the sample surface of (c) SC45 at $\varepsilon = 5.2\%$ and (d) PS45 specimens at $\varepsilon = 7.2\%$, respectively.

Figure 7 Relationship between resolved shear stress for basal slip system at yielding and the angle ϕ which is defined as the initial angle between loading axis and $[0001]$ direction.

Figure 8 Finite element mesh and boundary conditions used in the present analysis.

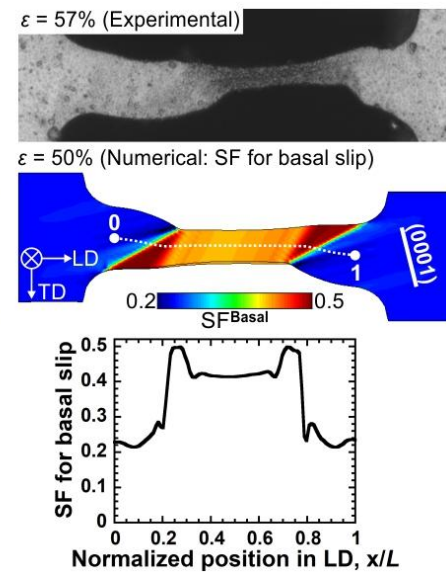
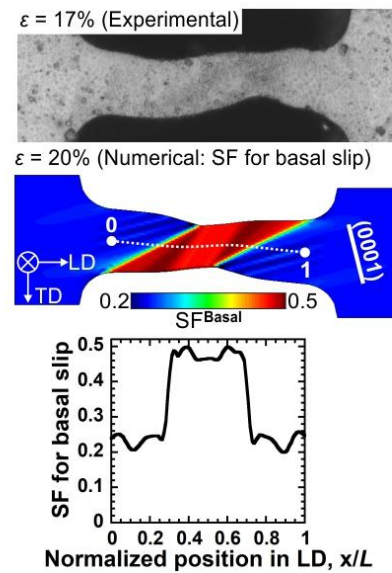
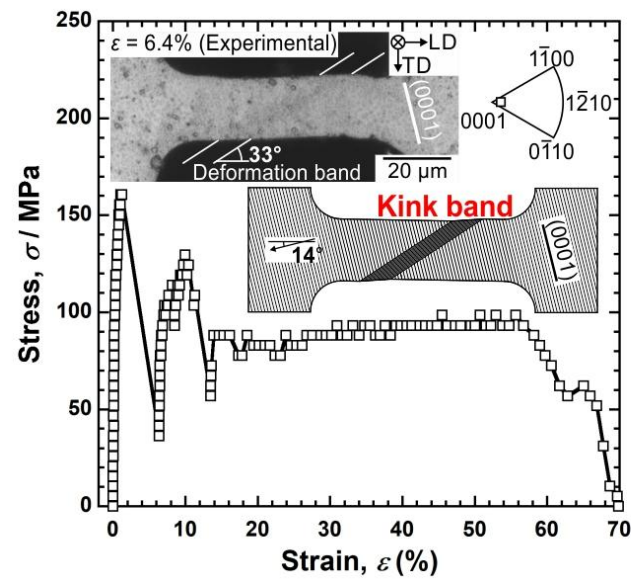
Figure 9 Experimental and calculated stress-strain curves with calculated distributions of accumulated basal slip at $\varepsilon = 3.0\%$, 6.0% , 10.0% and 50.0% .

Figure 10 (a) Calculated change in the angle ϕ between loading axis and $[0001]$ direction at a middle position in the analysis model. Calculated distributions of angle ϕ at (b) $\varepsilon = 3.0\%$ and (c) $\varepsilon = 6.0\%$. (d) Calculated change in the

Schmid factor for basal slip system at a middle position in the analysis model.

Figure 11 Calculated distributions of angle ϕ at (a) $\varepsilon = 10\%$, (b) $\varepsilon = 20\%$, and (c) $\varepsilon = 50\%$. Line profiles of angle ϕ from point “0” to point “1” on the model surface at (d) $\varepsilon = 10\%$, (e) $\varepsilon = 20\%$, and (f) $\varepsilon = 50\%$.

Figure 12 Calculated distributions of the Schmid factor for basal slip system at (a) $\varepsilon = 10\%$, (b) $\varepsilon = 20\%$, and (c) $\varepsilon = 50\%$. Line profiles of the Schmid factor for basal slip system from point “0” to point “1” on the model surface at (d) $\varepsilon = 10\%$, (e) $\varepsilon = 20\%$, and (f) $\varepsilon = 50\%$.



Highlights:

1. Ductility of LPSO single crystals strongly depends on loading direction.
2. Remarkable ductility of LPSO crystals was achieved where a kink band was formed.
3. Numerical analysis reproduced deformation behavior of a LPSO single crystal.
4. Changes in Schmid factor by lattice rotation lead to the remarkable ductility.

Table 1 Critical resolved shear stress for basal slip of 18R-type LPSO phase.

Material	Method	Specimen size	CRSS for basal slip	References
Polycrystal	Compression	$2 \times 2 \times 5 \text{ mm}^3$	10–30 MPa	[7, 16]
Single crystal	Compression	$7 \times 7 \text{ }\mu\text{m}^2$	12–13 MPa (Aspect ratio of height: 2–4)	[48]
Single crystal	Compression	$\Phi 3.5\text{--}3.8 \text{ }\mu\text{m}$	23 MPa (Aspect ratio of height: 2–2.3)	[50]
Single crystal	Bending	$50 \times 10 \times 20 \text{ }\mu\text{m}^3$	27–30 MPa	[49]
Single crystal	Tension	$50 \times 20 \times 20 \text{ }\mu\text{m}^3$	9.4 MPa	[41]
Single crystal	Tension	$50 \times 20 \times 20 \text{ }\mu\text{m}^3$	25-29 MPa (Upper yield) 12-19 MPa (Lower yield)	This study This study
Pre-strained single crystal	Tension	$50 \times 20 \times 20 \text{ }\mu\text{m}^3$	15 MPa	This study

Table 2 Material parameters for basal slip system (unit in MPa).

τ_0	τ_1	θ_0	θ_1
35	0.0001	10	30

Figure01

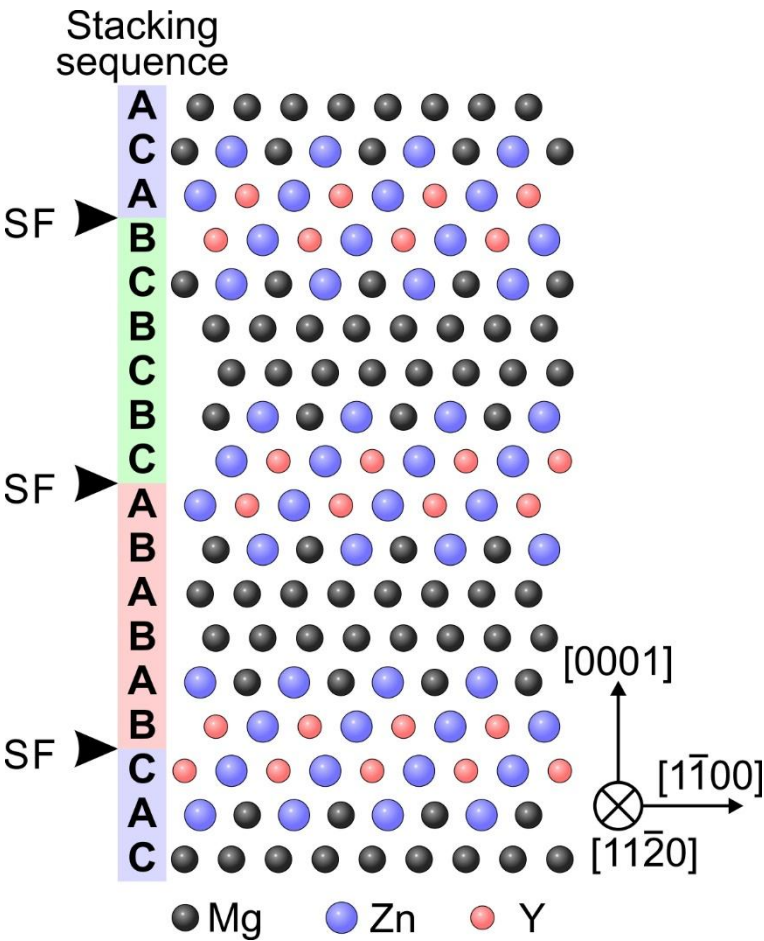


Figure02

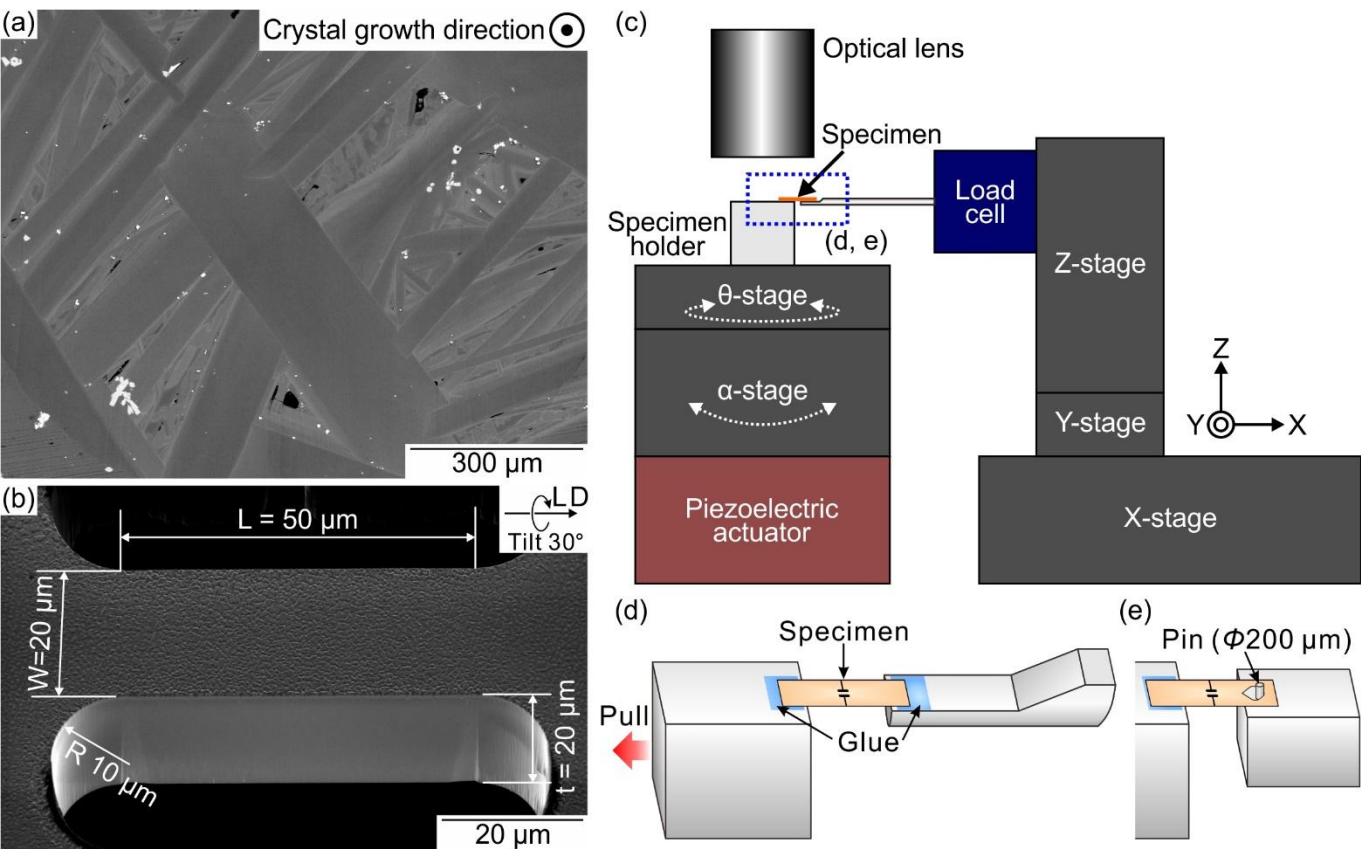


Figure03

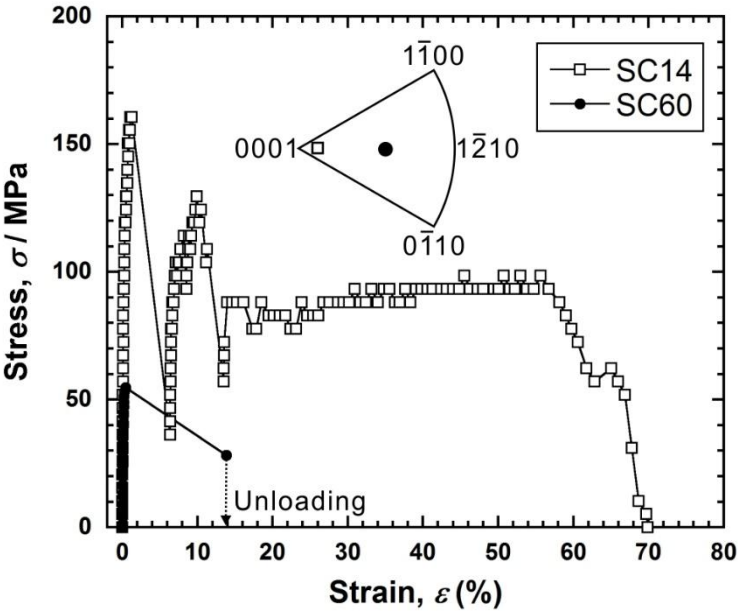


Figure04

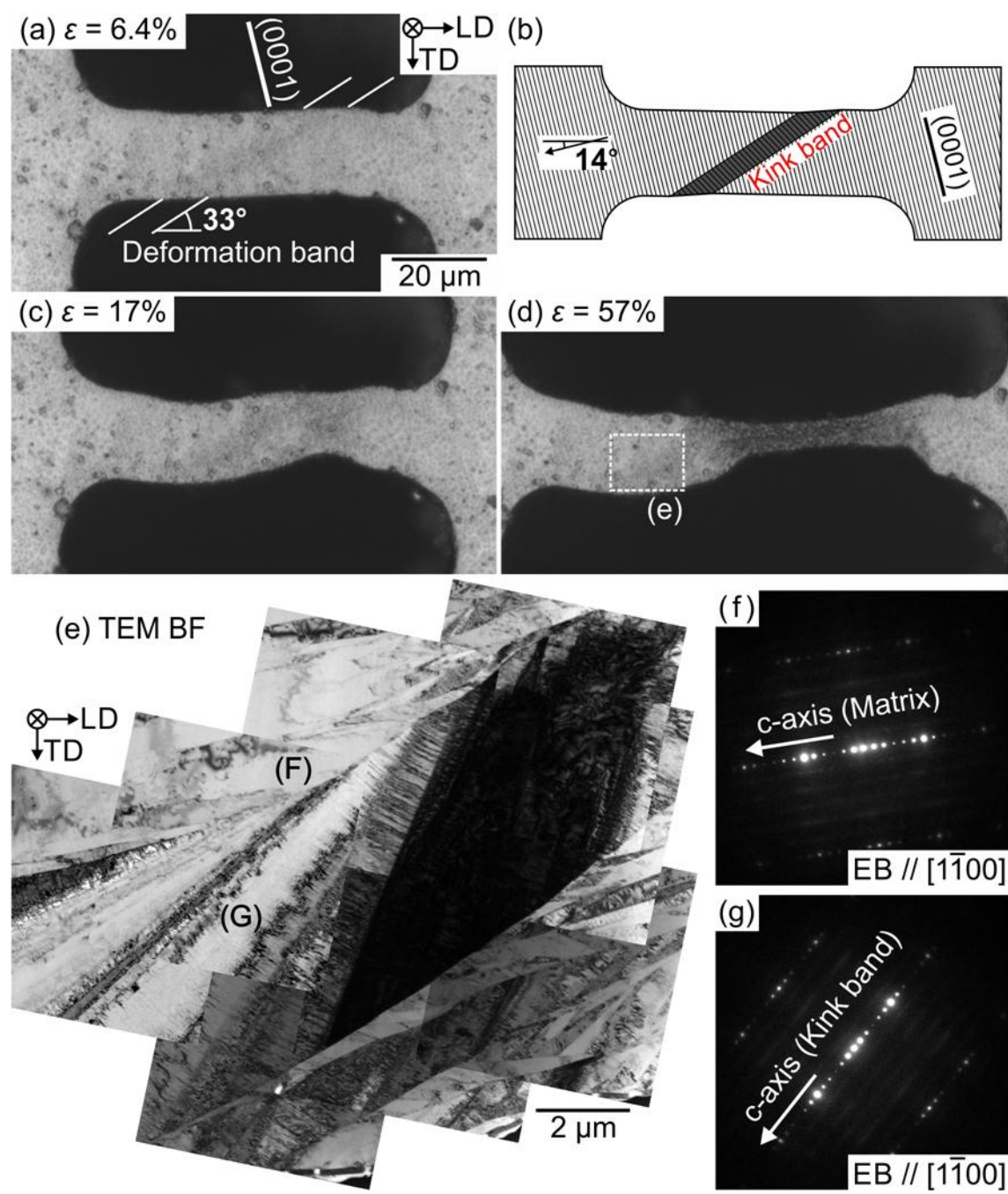


Figure05

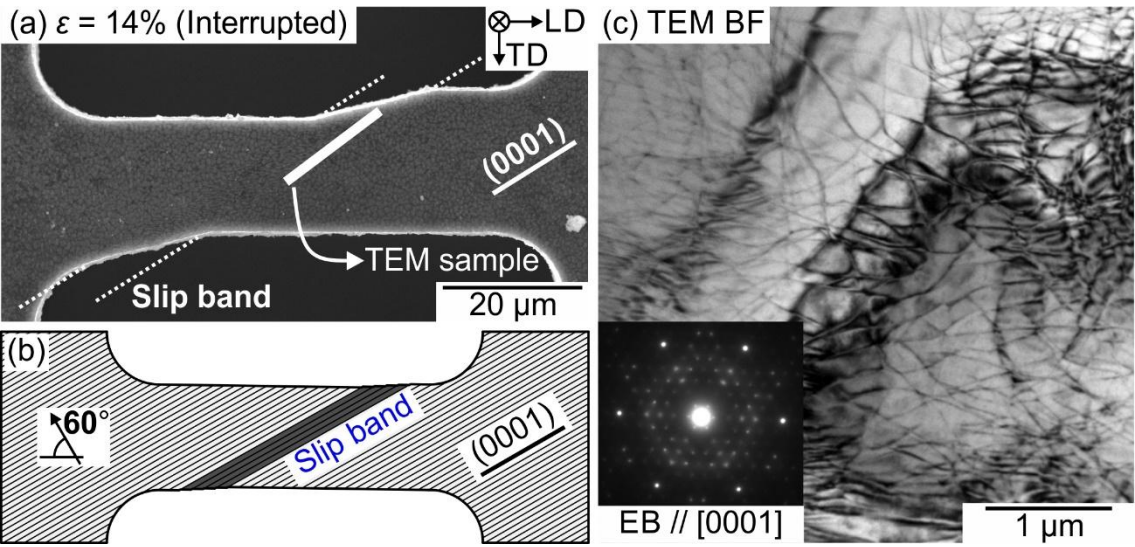


Figure06

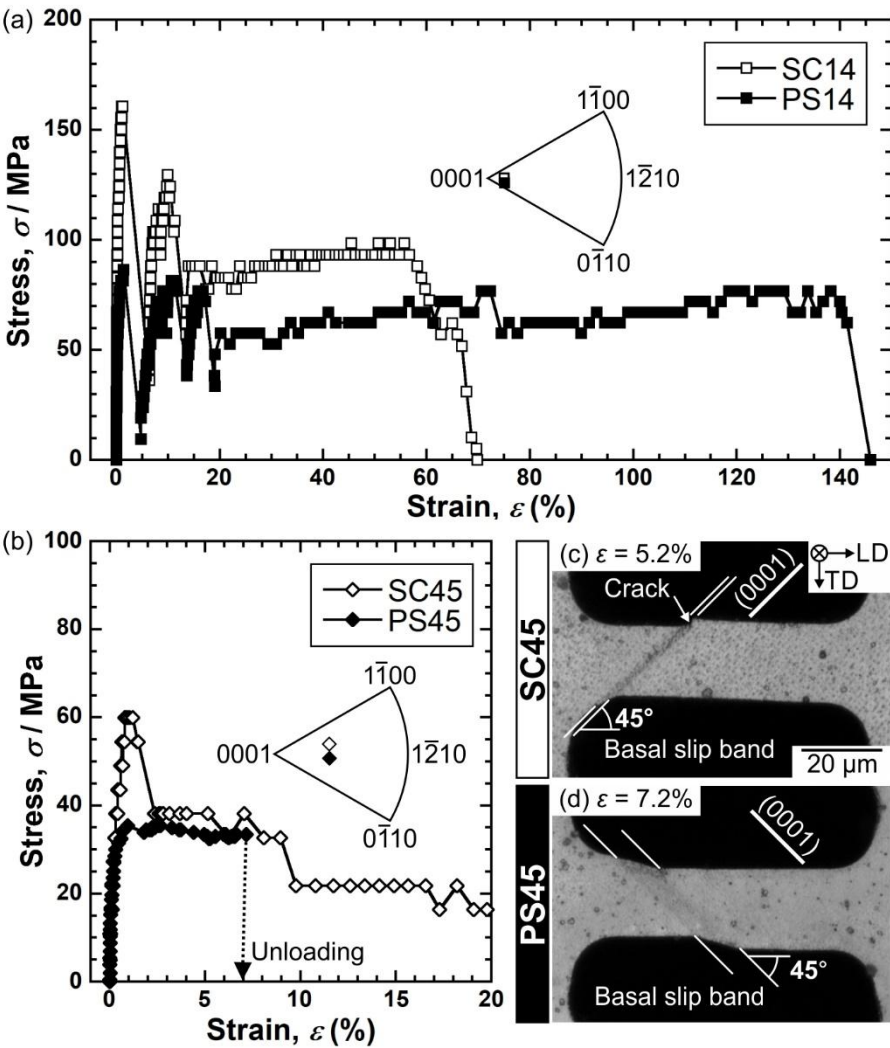


Figure07

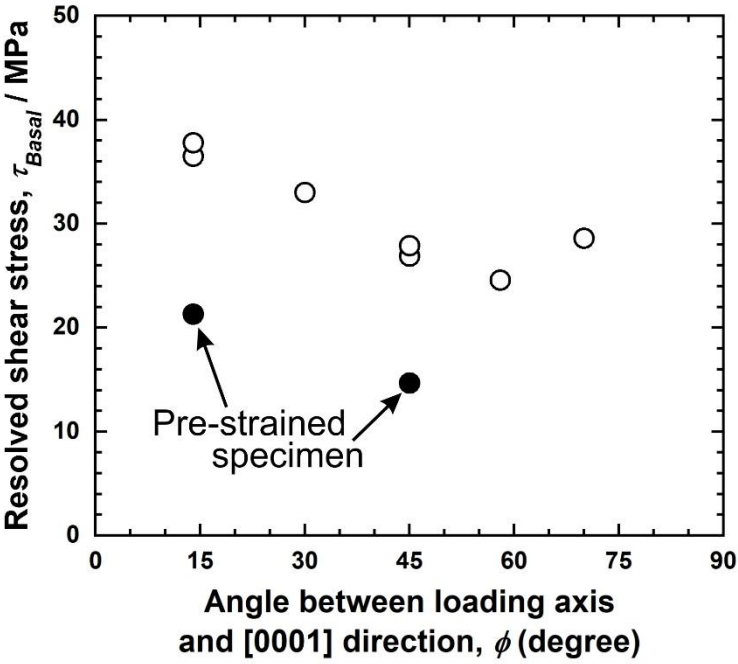


Figure08

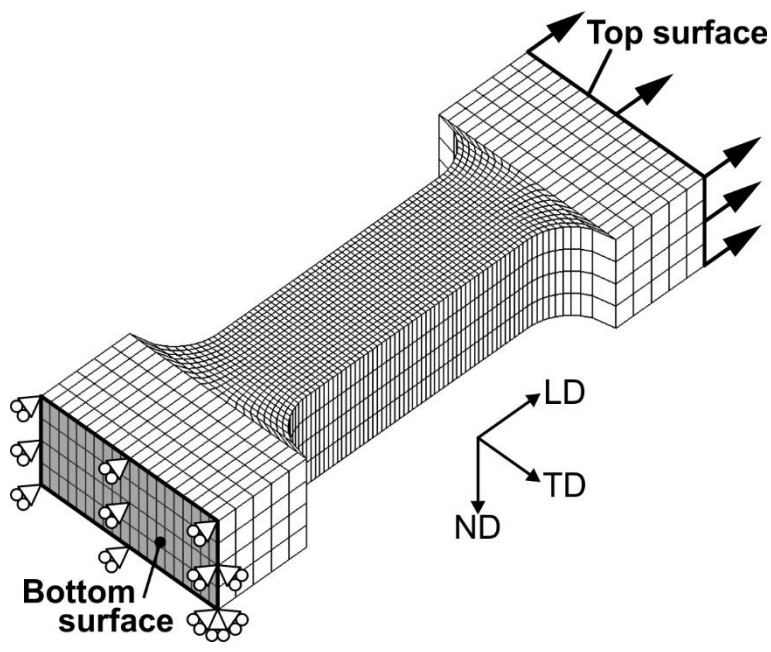


Figure09

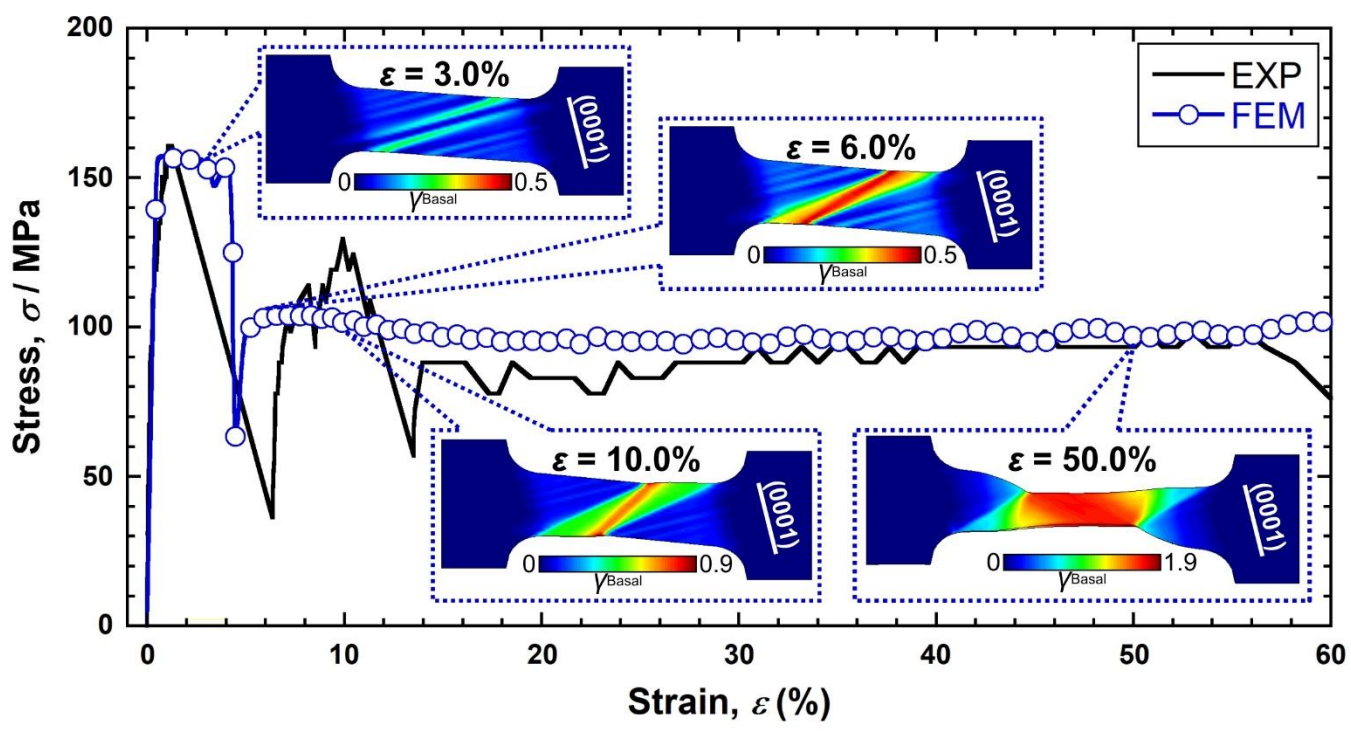


Figure10

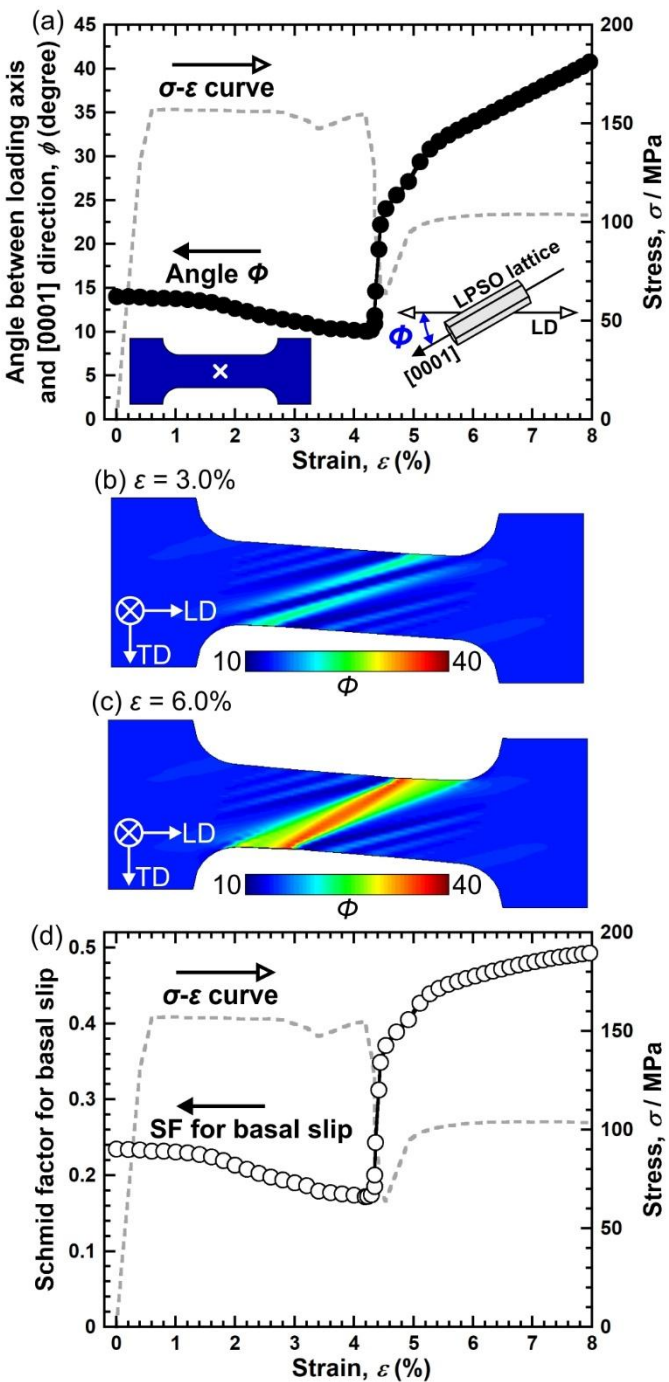


Figure11

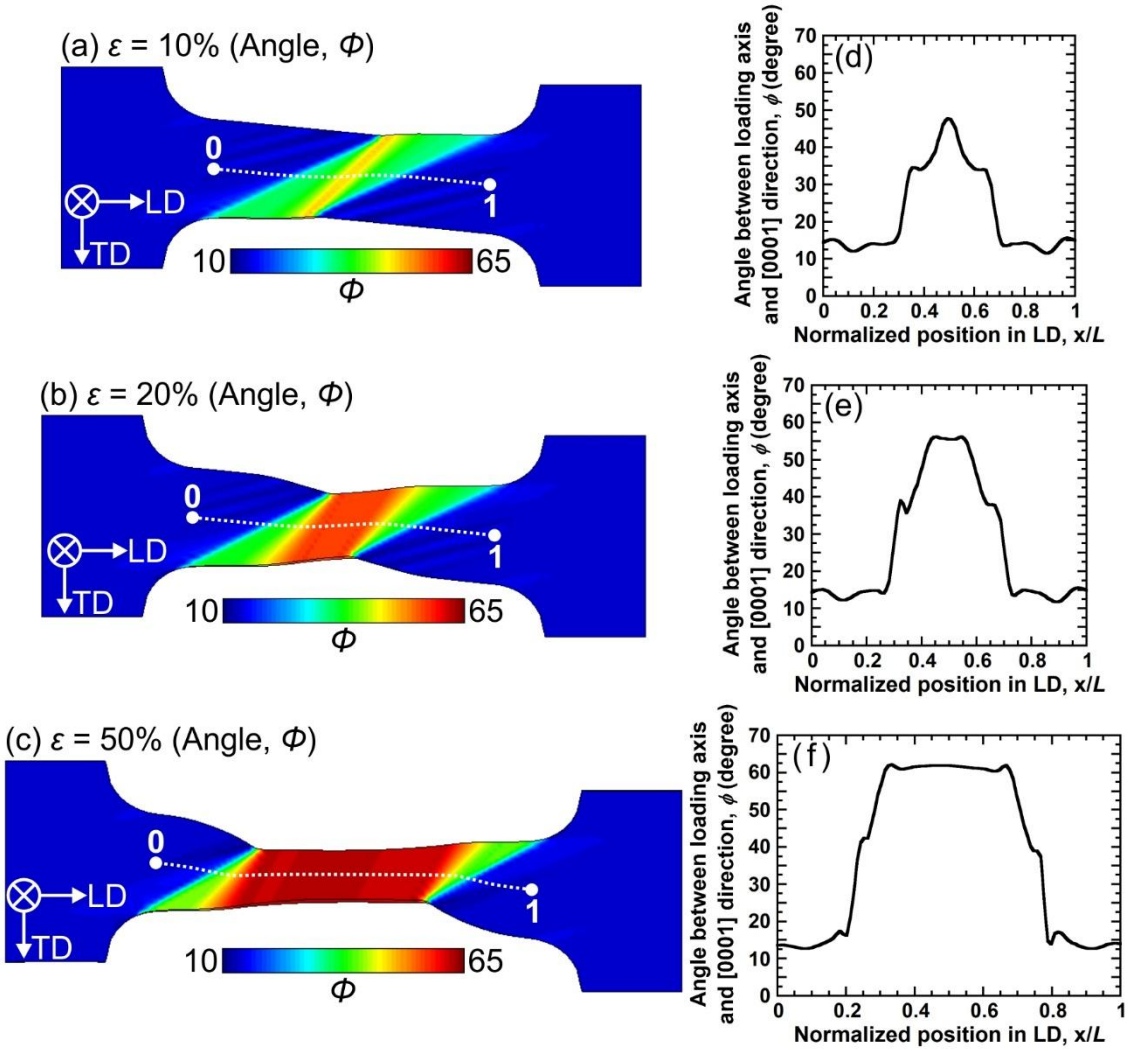


Figure12

